Materials Science in Semiconductor Processing 81 (2018) 127–138

Contents lists available at ScienceDirect

Materials Science in Semiconductor Processing

journal homepage: www.elsevier.com/locate/mssp

Heterogeneous SnO_2/ZnO nanoparticulate film: Facile synthesis and humidity sensing capability

A.S. Ismail[a], M.H. Mamat[a,b,*], M.F. Malek[a,b], M.M. Yusoff[a,c], R. Mohamed[a,d], N.D. Md. Sin[a], A.B. Suriani[e], M. Rusop[a,b]

[a] NANO-ElecTronic Centre (NET), Faculty of Electrical Engineering, Universiti Teknologi MARA (UiTM), 40450 Shah Alam, Selangor, Malaysia
[b] NANO-SciTech Centre (NST), Institute of Science (IOS), Universiti Teknologi MARA (UiTM), 40450 Shah Alam, Selangor, Malaysia
[c] Kulliyyah of Engineering, International Islamic University Malaysia (IIUM), 50728 Kuala Lumpur, Malaysia
[d] Faculty of Applied Sciences, Universiti Teknologi MARA (UiTM), 26400 Bandar Jengka, Pahang, Malaysia
[e] Nanotechnology Research Centre, Faculty of Science and Mathematics, Universiti Pendidikan Sultan Idris (UPSI), 35900 Tanjung Malim, Perak, Malaysia

ARTICLE INFO

Keywords:
Immersion
ZnO
ZnO/SnO2
Tin oxide
Heterojunction
Humidity sensor

ABSTRACT

Highly sensitive and extremely thin tin oxide/zinc oxide (SnO_2/ZnO) heterojunction films were prepared via a two-step solution-based method for humidity-sensing application. The average diameters of the ZnO and SnO_2 nanoparticles were 26 and 6 nm, respectively. The deposition of SnO_2 for 3 min reduced film resistance from 6.74 MΩ to 0.40 MΩ. Remarkably, the humidity-sensing performance of the heterojunction sensors was critically dependent on deposition time, and sensors subjected to 3 min deposition exhibited the highest sensitivity (90.56) to humidity, which was significantly higher than that of bare ZnO. This study indicates that the use of SnO_2/ZnO heterojunction has a great potential in humidity sensing applications.

1. Introduction

Humidity is a term commonly associated with water content in vapor or gas form. Despite the necessity of water in human life, uncontrollable humidity levels can cause disasters. Therefore, humidity sensors are of practical importance. In semiconductor industries, humidity sensors are used in wafer-processing areas [1]. In medical applications, humidity sensors are used in monitoring human breathing [2–7]. Furthermore, by monitoring breathing airflow, some respiratory disorders and failures, such as hypopnea and apnea can be identified [8]. Some major diseases can be diagnosed by observing abnormal respiratory rates [9]. In agricultural sectors, humidity sensors are applied in monitoring crop growth. Data from the humidity sensors are directly transferred to a central control system integrated into a wireless sensor network technology. Detailed information, such as water leakage, soil moisture, air humidity, and air pressure, can be collected [10,11]. Studies on humidity sensors mostly focused on high sensitivity over broad range of humidity level, good reproducibility, low cost, ease of fabrication, and long-term stability of the sensors [12–14]. Metal oxides, such as titanium dioxide (TiO_2), tin oxide (SnO_2), zinc oxide (ZnO), and iron oxide (Fe_2O_3), were reported suitable to the production of high-quality humidity sensors [15–19]. In addition, these metal oxides can also be used for other sensor applications such as formaldehyde and ethanol sensors [20,21].

Several researchers investigated the functionalities of heterostructure metal oxide films for various applications. For instance, Taleatu et al. demonstrated that decorating TiO_2 nanoporous films with a thin ZnO layer improves the photocatalytic properties of the films [22]. Implementing heterostructure metal oxides for solar cell application enhances electron transport properties and reduces the chance of charge recombination [23]. In thin film transistor applications, Nam et al. revealed that the synergetic interaction of ZnO/SnO_2 layer produced excellent carrier mobility, caused by an exceptional interface structure [24]. SnO_2 and ZnO are ideal for heterojunction-based devices because of their wide energy band gap, high sensitivity to humidity changes, high thermal stability, and nontoxicity [25–27]. Meanwhile, studies on the use of heterostructure metal oxides for humidity-sensing applications are currently limited. In recent studies, researchers mostly

---

* Corresponding author at: NANO-ElecTronic Centre (NET), Faculty of Electrical Engineering, Universiti Teknologi MARA (UiTM), 40450 Shah Alam, Selangor, Malaysia.
E-mail address: mhmamat@salam.uitm.edu.my (M.H. Mamat).

https://doi.org/10.1016/j.mssp.2018.03.022
Received 28 October 2017; Received in revised form 7 February 2018; Accepted 17 March 2018

focused on the utilization of nanostructure-based sensors instead of nanoparticulate-based humidity sensors. Narimani et al. fabricated ZnO nanorod-based humidity sensor through a chemical bath deposition method [28]. The synthesized humidity sensor had approximately 10 µm thick, and its sensitivity was 61.23%. Azad et al. prepared a 1.8–2.5 µm ZnO nanorod-coated optical fiber humidity sensor that exhibited a sensitivity of − 68 (count/% relative humidity (RH)) [29]. However, the use of nanostructure-based humidity sensors produced thick films and required longer deposition time.

In this study, highly sensitive and extremely thin SnO_2/ZnO heterojunction films (167–294 nm) for humidity-sensing applications were prepared through a two-step solution-based method. The structural, optical, electrical, and humidity-sensing performance of the films were extensively studied at different deposition times of SnO_2. Controlling the deposition time of secondary layers is crucial to the optimization of film thickness for the enhancement of the heterojunction structures of the films. We attempted to fabricate a thin heterojunction film that can exhibit excellent humidity-sensing performance.

2. Experimental procedure

2.1. Preparation of ZnO film

Two solution-based methods were used for the deposition of SnO_2/ZnO films. In particular, the deposition of the ZnO and SnO_2 layers was conducted through a spin-coating and immersion methods, respectively. For the deposition of ZnO film, a 0.4 M zinc acetate dihydrate ($Zn(CH_3COO)_2{\cdot}2H_2O$; 98% purity; Sigma-Aldrich) and 0.004 M aluminum nitrate nonahydrate ($Al(NO_3)_3{\cdot}9H_2O$; 98% purity; Sigma-Aldrich) were used as starting materials. Monoethanolamine (0.4 M; MEA, $H_2NCH_2CH_2OH$; 99% purity; Sigma-Aldrich) was added as a stabilizing agent. The reagents were then dissolved in 100 mL of 2-methoxyethanol. The solution was stirred on a hot plate stirrer for 3 h at 80 °C and then stirred for 24 h at room temperature to attain a homogeneous solution. The resulting solution was deposited onto a glass substrate via the spin-coating method at a speed of 3000 rpm for 1 min. The coated glass substrate was then dried at 150 °C for 10 min for the evaporation of the solvent. The coating process was repeated five times to achieve the desired thickness. Then, the ZnO-coated substrate was annealed for 1 h at 500 °C in air.

2.2. Preparation of SnO_2/ZnO heterojunction film

For the deposition of the SnO_2/ZnO heterojunction film, 0.02 M tin (IV) chloride pentahydrate ($SnCl_4{\cdot}5H_2O$; 98% purity; Sigma-Aldrich) was used as starting material, 0.05 M hexamethylenetetramine (HMT, $C_6H_{12}N_4$; 99% purity; Sigma-Aldrich) as stabilizer, and 0.1 M NaOH (99% purity; Systerm) as neutralizer. The reagents were dissolved in 250 mL of DI water and sonicated in ultrasonic water bath for 30 min at 50 °C. Then, the solution was stirred on a magnetic hot plate stirrer for 3 h at room temperature until a clear solution was obtained. Subsequently, the solution was poured into a Scott bottle, in which the ZnO coated substrate was placed at the bottom of the bottle. The deposition of the SnO_2 layer was performed for 1, 3, 5, and 15 min at room temperature. The prepared SnO_2/ZnO heterojunction film was dried for 10 min at 150 °C, followed by annealing for 1 h at 500 °C. The configuration of the SnO_2/ZnO-based humidity sensors were finalized by depositing 60 nm of gold (Au) as contact electrode with a sputter coater (Emitech K550X) and physical mask, as shown in Figs. 1(a) and 1(b).

2.3. Characterizations

The structural properties of the SnO_2/ZnO films were characterized with field emission scanning electron microscopy (FESEM; JEOL JSM-7600F) and high-resolution transmission electron microscopy (HR-TEM; JEM-ARM200F). For the preparation of a TEM sample, a part of the SnO_2/ZnO film prepared through 5 min SnO_2 deposition was scratched with a sharp tool and then placed on top of a copper grip for further analysis. The elemental analysis of the SnO_2/ZnO film was characterized using energy-dispersive X-ray spectroscopy (EDS, Oxford Instruments Inca X-Act). The crystalline properties of SnO_2/ZnO films were characterized through X-ray diffraction measurement (XRD; PANalytical X'Pert PRO). The structural properties of SnO_2/ZnO films were characterized using Raman spectroscopy with an argon (Ar) laser operating at 514 nm as excitation source (Horiba Jobin Yvon-79 DU420A-OE-325). The optical properties of the SnO_2/ZnO films were investigated with an ultraviolet–visible (UV–vis) spectrophotometer (Varian Cary 5000). The current–voltage (I–V) characteristics of the SnO_2/ZnO films were measured with a two-probe I–V measurement system (I–V, Advantest R6243). The sensor performance of the SnO_2/ZnO-based humidity sensor was characterized with a humidity chamber (ESPEC-SH261) equipped with a sensor measurement system (Keithley 2400).

3. Result and discussion

3.1. Structural and morphological characteristics

The structure of the films were inspected from the surface and cross-sectional images using FESEM. Fig. 2(a–j) depicts the surface structure of the uncoated ZnO, SnO_2 and SnO_2/ZnO films at 50,000× and 100,000× magnifications. The surface images of ZnO and SnO_2 are shown in Figs. 2(a) and 2(b), respectively, which indicate that the nanoparticles were uniformly distributed across the substrate. The average diameter of the ZnO nanoparticles was approximately 26 nm. The high-magnification image displayed the appearance of pores on the surface of ZnO. Figs. 2(c) and 2(d) depicts the 1 min deposition of SnO_2/ZnO. The SnO_2 layer was uniformly laminated on the ZnO surface, and the surface of the SnO_2/ ZnO subjected to 1 min deposition consisted of white and dark regions which may due to the different thickness of the regions. As the deposition times of SnO_2 increased from 3 min to 15 min (Fig. 2(e–j)), the whitish and dark regions gradually disappeared. The average diameter of SnO_2 (approximately 6 nm) was

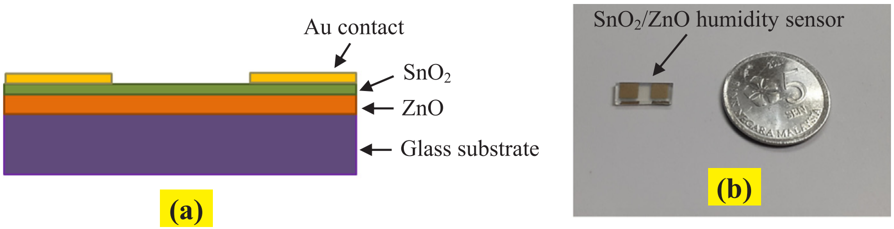

Fig. 1. (a) Configuration and (b) the actual image of SnO_2/ ZnO heterojunction-based humidity sensor.

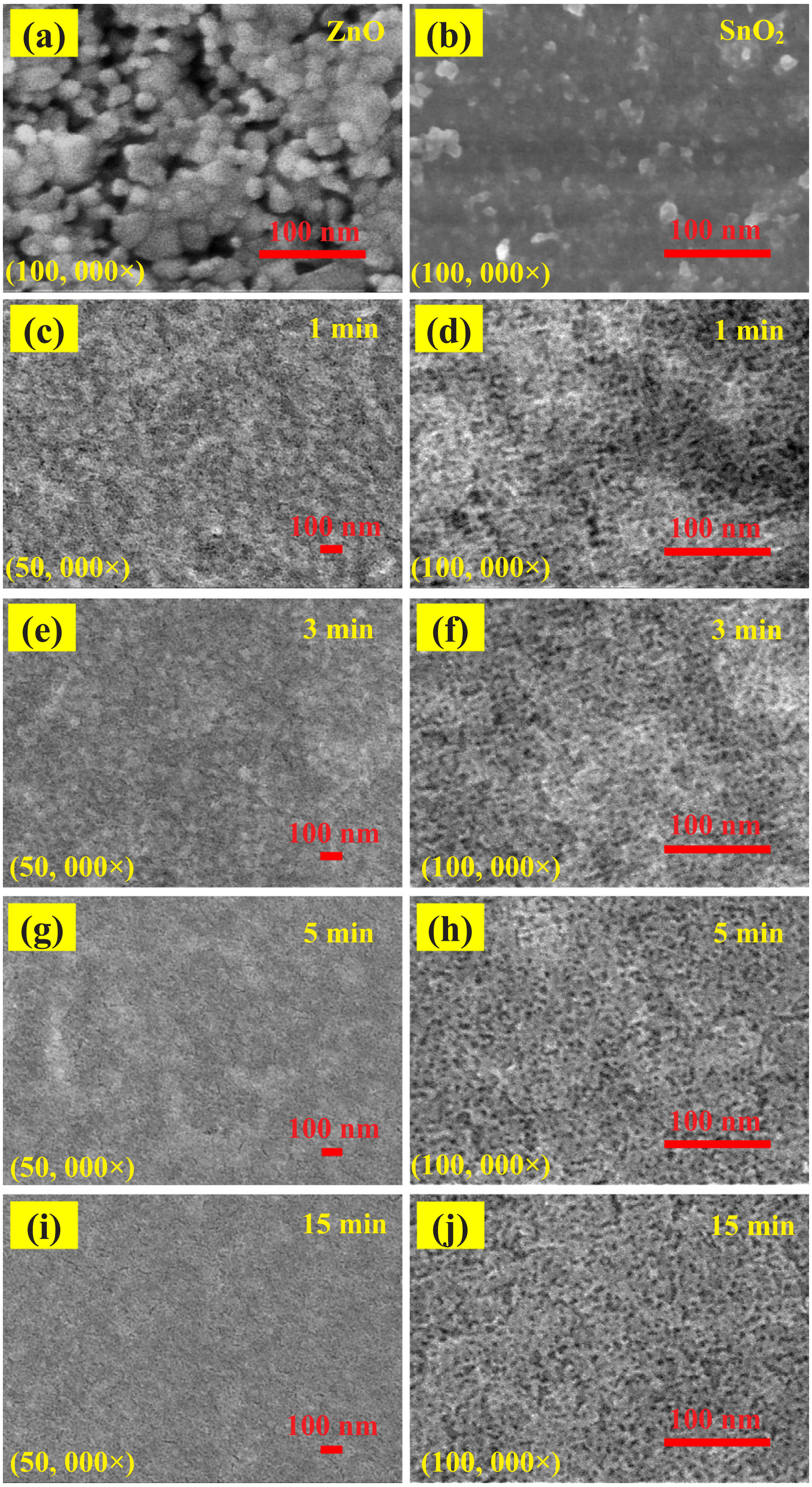

Fig. 2. Surface images of (a) ZnO and (b) SnO_2 at 100,000× magnification. Surface images of SnO_2/ZnO deposited with SnO_2 for (c-d) 1 min, (e-f) 3 min, (g-h) 5 min, and (i-j) 15 min at 50,000× and 100,000× magnifications.

independent of deposition time. Fig. 3(a–e) show the cross-sectional images at 50,000× magnification of the ZnO and SnO_2/ZnO films. The intimate interfacial contact between the oxide layers is also displayed. The average thickness of the films was dependent on SnO_2 deposition time, increasing from 167 nm to 188, 206, 211, or 294 nm for 1, 3, 5, or 15 min deposition, respectively. Fig. 3(f) shows a corresponding EDS spectrum, which confirms the presence of Zn, Sn, and O elements. According to the EDS spectrum, the peaks of Zn, Sn, and O correspond

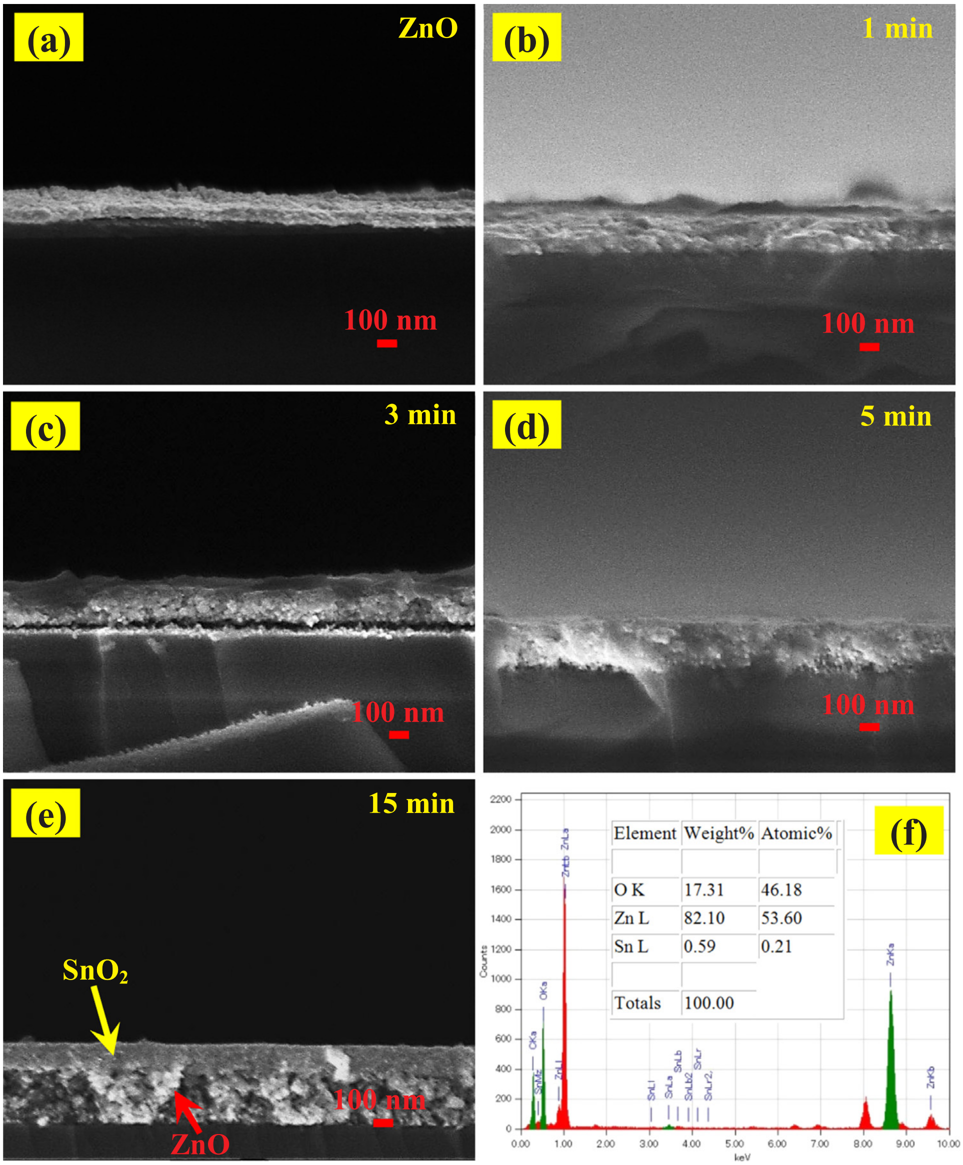

Element	Weight%	Atomic%
O K	17.31	46.18
Zn L	82.10	53.60
Sn L	0.59	0.21
Totals	100.00	

Fig. 3. The cross-sectional images at 50,000× magnification of (a) ZnO and SnO_2/ZnO deposited with SnO_2 for (b) 1, (c) 3, (d) 5, and (e) 15 min (f) EDS spectra of SnO_2/ZnO heterojunction film exhibiting the existence of Sn, Zn, and O elements.

to an atomic ratio of 53.60:0.21:46.18. The surface of the SnO_2 heterolayer became increasingly smooth as the deposition times increased possibly because the SnO_2 nanoparticles filled the pore areas between the ZnO nanoparticles. Upon further increase of deposition time, the SnO_2 nanoparticles continued to form continuous layers on top of the ZnO film, forming a smooth surface. This phenomenon is shown in the schematic diagram in Fig. 4(a-c).

HR-TEM was performed for the analysis of the configuration of SnO_2/ZnO. The configuration was examined for the availability of both ZnO and SnO_2 crystals (Fig. 5). Fig. 5(a) depicts the low-magnification HR-TEM image of the SnO_2/ZnO heterojunction film. The configuration of SnO_2/ZnO in a heterostructured-film form is unnoticeable because the scratch method was used, which may probably damage the film. Besides, the image consists of dark and overlapping bright regions.

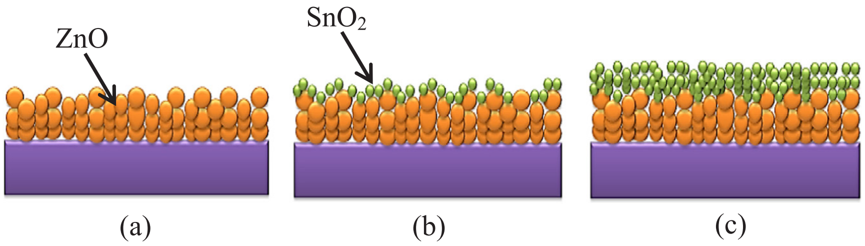

Fig. 4. Schematic diagram of (a) ZnO and SnO_2/ZnO deposited for (b) lower and (c) higher deposition times.

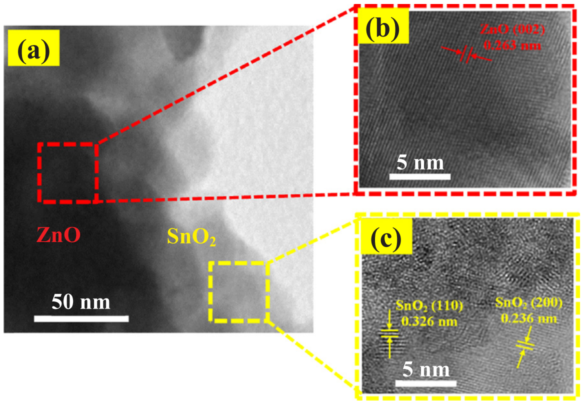

Fig. 5. (a) Low-magnification TEM image of SnO_2/ZnO heterojunction film. High-magnification TEM images of (b) ZnO and (c) SnO_2 region.

High-magnification images of some parts of the dark and bright regions were obtained for the observation of the planes of the crystal structure present (Fig. 5(b) and (c)). One lattice fringe of 0.263 nm, corresponding to the (002) plane of the hexagonal ZnO structure, and two different lattice fringes of 0.236 and 0.326 nm (Fig. 5(d) and (e)), which corresponded to the (200) and (110) planes of the rutile SnO_2 structure, respectively, were observed from the high-magnification HR-TEM images. These results indicate that the nanoparticles appearing in the FESEM images consist of ZnO and SnO_2 crystals.

The crystalline properties of the ZnO and SnO_2/ZnO films were analyzed from the XRD pattern in Fig. 6(a). The XRD patterns were indexed to ZnO hexagonal wurtzite structure (zincite phase JCPDS 36-1451, Fig. 6(b)). One prominent peak was observed from the patterns, situated around 34.4° of the diffraction angle, which corresponds to the (002) plane orientation. The presence of this peak indicated that the ZnO crystal preferentially grew along the *c*-axis orientation. Other insignificant peaks were also evident and corresponded to the (100) and (101) plane orientation. No SnO_2 diffraction peak was observed on the pattern possibly because of the extremely low thickness or poor crystallinity of the SnO_2 layer. These properties limit X-ray detection. This result was also reported in another study [30]. In addition, Lee et al. reported that the crystallization of SnO_2 prepared through a solution-based method requires an extremely high annealing temperature ($> 500\,^\circ C$) because low annealing temperature tends to produce amorphous SnO_2 films [31]. The influences of SnO_2 layer deposition on heterostructured films were further analyzed by referring to the alteration that appears at the prominent diffraction peak (002). The crystallite size, *D*, of ZnO and SnO_2/ZnO was estimated by using the following equation [32]:

$$D = \frac{0.94\lambda}{\beta \cos\theta} \tag{1}$$

where λ is the X-ray wavelength (1.54 Å), β is the FWHM in radians, and θ is the diffraction angle. The values of β and θ obtained from (002) plane orientation are shown in Table 1. The crystallite sizes of the films with respect to (002) orientation are listed in Table 1. Apparently, the crystallite sizes slightly decreased from 33 nm to 25 nm as the SnO_2 layer was deposited for 1 min. As the deposition time of SnO_2 was increased further to 15 min, the crystallite sizes significantly reduced to 9 nm, which is more than three times smaller than that of ZnO film. Furthermore, the diffraction angles shifted from 34.38° to 34.94°, which was far from the standard relaxed ZnO crystal (34.4°). Thus, lattice strain/stress of the films was augmented. The strain along the *c*-axis orientation was estimated by using the following equation [33]:

$$\varepsilon_{zz} = \frac{c_{film} - c_{bulk}}{c_{bulk}} \times 100\% \tag{2}$$

where c_{film} is the lattice parameter corresponding to (002) plane orientation of the films, and c_{bulk} is the lattice parameter (strain free) of bulk ZnO with a value of 5.2066 Å. The lattice constant of the films can be extracted from the following equation [34]:

$$\frac{1}{d^2} = \frac{h^2 + k^2 + l^2}{c^2} \tag{3}$$

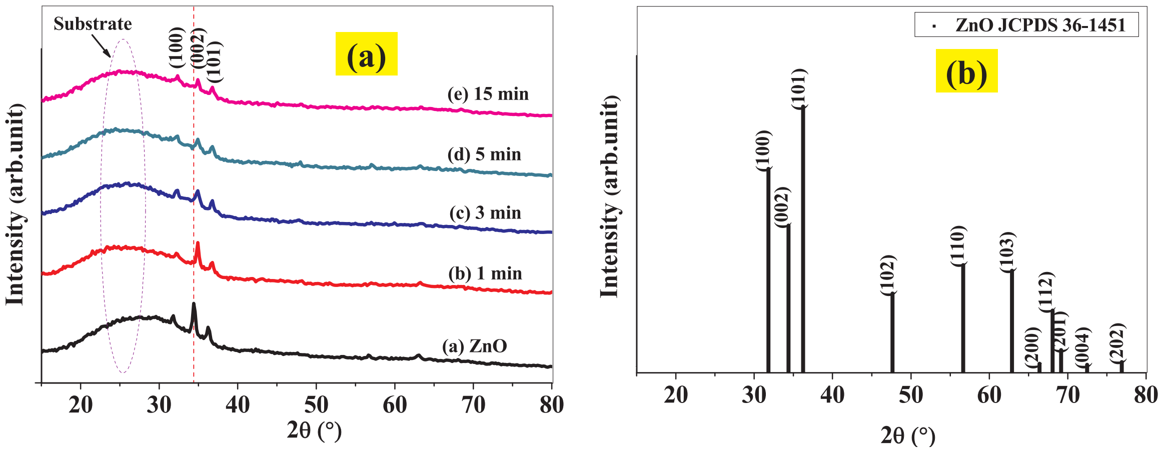

Fig. 6. (a) XRD pattern of ZnO and SnO_2/ZnO heterojunction at different deposition times of SnO_2. (b) Standard XRD pattern of ZnO powder (JCPDS 36–1451).

Table 1
Diffraction angle at (002) plane orientation, $FWHM_{(002)}$, crystallite size, interplanar distance, c_{film}, strain, and stress of ZnO and SnO_2/ZnO heterojunction films at different deposition times of SnO_2.

Sample	2*θ* at (002) plane (deg)	$FWHM_{(002)}$ (deg)	Crystallite size (nm)	Interplanar distance,*d* (Å)	c_{film} (Å)	Strain (%)	Stress (GPa)
ZnO	34.38	0.265	33	2.6054	5.2108	0.080	− 0.19
1 min	34.77	0.343	25	2.5771	5.1541	− 1.008	2.35
3 min	34.78	0.476	18	2.5763	5.1527	− 1.035	2.41
5 min	34.84	0.552	15	2.5720	5.1441	− 1.200	2.80
15 min	34.94	0.923	9	2.5649	5.1298	− 1.475	3.44

where (*hkl*) is the Miller index and d is the interplanar spacing between the adjacent lattice planes of ZnO.

$$c_{film} = \frac{\lambda}{\sin\theta} \tag{4}$$

The values of ε_{zz}, d, and c_{film} are presented in Table 1. The positive and negative signs of ε_{zz} represent the strain quantity in stretched and compressed conditions, respectively. The strain values metamorphosed from tensile to compressive strain after coating with SnO_2, and the compressive stress of the SnO_2/ZnO films slightly increased together with the increase of SnO_2 layer thickness. The decrease of crystallite sizes may have promoted the increase in thickness because larger crystallite size induced lower-strained films [35]. Moreover, the decrease of d and c_{film} values were also in agreement with the reduction of crystallite size and enhancement of film strain. The residual stress of the films due to the increase of the SnO_2 layer thickness was analyzed, and the residual stress, σ_{film}, of the hexagonal crystal was determined by the following biaxial stress expression [36]:

$$\sigma_{film} = \frac{2C_{13}^2 - C_{33}(C_{11} + C_{12})}{2C_{13}}\varepsilon_{zz} \tag{5}$$

where ε_{zz} is the film strain and C_{ij} is the elastic stiffness constant of bulk ZnO. The included value of C_{ij} were as follows: C_{11} = 208.8 GPa, C_{33} = 213.8 GPa, C_{12} = 119.7 GPa, and C_{13} = 104.2 GPa resulted in the following numerical correspondence: $\sigma_{film} = -233\varepsilon_{zz}$ (GPa). The film stresses shown in Table 1 indicated that the residual stress of the ZnO film was compressive (negative sign), whereas the SnO_2/ZnO films produced tensile stress (positive sign). The thick SnO_2 layer produced a large tensile stress value. On the basis of the study by Malek et al., we concluded that the ZnO nanoparticle films synthesized at 500 °C tend to possess low residual tensile strain and compressive stress [37]. Additionally, the transformation of strain/stress direction and the enhancement of thin film strain/stress at prolonged SnO_2 deposition time may be caused by the following factors: lattice mismatch between ZnO and SnO_2 layers [35,38] because of interplanar distance difference, and the possible diffusion or segregation of Sn atoms into the ZnO lattice at the bilayer interface during the annealing process, leading to the deterioration of ZnO lattice [39]. According to Nam et al., the synthesis of ZnO/SnO_2 heterojunction forms three consecutive regions, namely, the Sn region, Zn–Sn mixed region, and Zn region, through which the atoms from the coated layer (SnO_2) diffuse into the existing layers (ZnO) at the interface region [24]. On the basis of our findings, we concluded that the residual tensile stress enlargement is proportional to the thickness of SnO_2 layer, and this enlargement may be triggered by increased diffusion of Sn. The decrease in grain size because of the increase in the thickness of the SnO_2 layer results in a large grain boundary specific area and thus increases interface-related deficiencies [40].

The SnO_2/ZnO heterojunction film was characterized by Raman spectroscopy to further confirm the presence of ZnO and SnO_2 nanoparticles. Fig. 7 shows the Raman spectrum of SnO2/ZnO heterojunction film. Three typical SnO_2 characteristic peaks of A_{1g} vibration mode, A_{1g} symmetric breathing mode, and A_{2u} IR active vibration mode were observed at Raman shift of 616, 545, and 680 cm^{-1}, respectively [41]. In addition, one ZnO spectral peak at 441 cm^{-1} corresponding to E_2(high) mode of the wurtzite phase, was also observed in the Raman spectrum [42]. This result indicates that both of ZnO and SnO_2 nanoparticles coexist in SnO_2/ZnO heterojunction film, which is consistent with HR-TEM results.

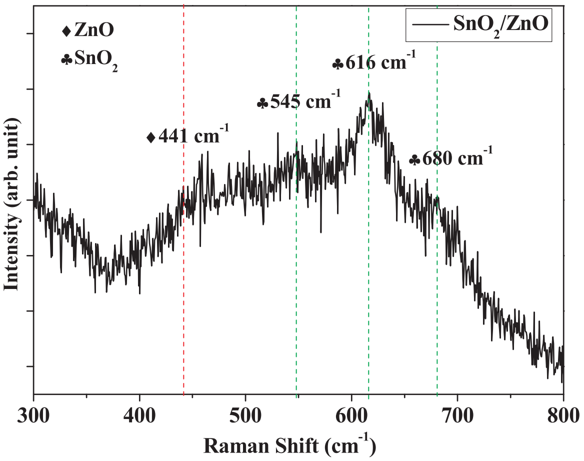

Fig. 7. Raman spectrum of SnO_2/ZnO heterojunction film.

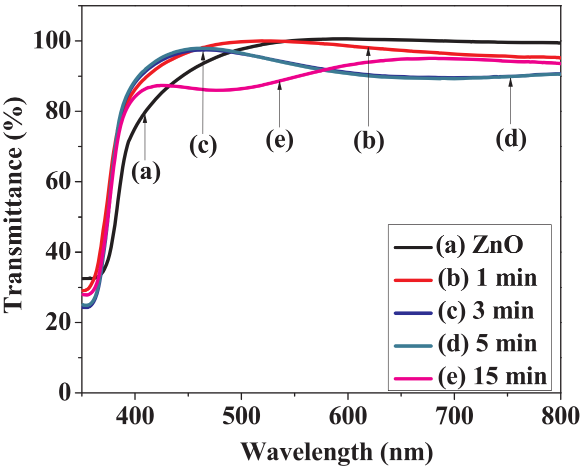

Fig. 8. Transmittance properties of ZnO and SnO_2/ZnO heterojunction at different deposition times of SnO_2.

3.2. Optical properties

Fig. 8 depicts the optical transmittance properties of the films measured using an UV–vis spectrophotometer in the range of 350–800 nm. All films exhibited good transmittance properties at the visible region, showing a sharp band edge at approximately 400 nm. This band edge corresponded to the band gap energy of ZnO and SnO_2 during the electron transition from the valence band to the conduction band. The average transmittance is shown in Table 2. All the films exhibited high transparency, and ZnO had the highest average transmittance (97.39%). The average transmittance was reduced to 97.07% after the films were subjected to deposition with SnO_2 for 1 min and continuously reduced to 92.27%, 91.96%, and 91.27% after 3, 5, and 15 min deposition, respectively. This phenomenon is well understood by using Beer–Lambert law [43], in which the attenuation of light is proportionally related to the path length (thickness) and concentration of an absorbing species. The reduction of transmittance may be correlate with the enhancement of the optical scattering leads and may be caused by the decreasing crystallinity along the *c*-axis and non-oriented SnO_2 crystal, as observed in XRD measurement [37]. Poor lattice structure orientation leads to high dispersion of light in grain

Table 2
Average transmittance, optical band gap energy and Urbach energy of ZnO and SnO_2/ZnO heterojunction films at different deposition times of SnO_2.

Sample	Average transmittance, T (%)	Optical band gap energy, E_g (eV)	Urbach energy, E_u (meV)
ZnO	97.39	3.260	57
1 min	97.07	3.285	66
3 min	92.27	3.290	70
5 min	91.96	3.280	91
15 min	91.27	3.275	108

boundaries [44]. The absorption coefficient, α, of the ZnO and SnO_2/ZnO films were determined by using Lambert's law [31].

$$a = \frac{1}{t}\ln\left(\frac{1}{T}\right) \tag{6}$$

where t is the thickness of the film, and T is the transmittance of the film. The absorption coefficient plot is shown in Fig. 9. The films exhibited high absorption in the UV region (< 400 nm). The considerable increase in light absorption in the UV region significantly was proportional to the increase of SnO_2 deposition time, which was related to the increase of the optical scattering effect.

The optical band gap energy, E_g, of the direct band gap ZnO and SnO_2 films as a function of film thickness is estimated using Tauc's relation as shown below [45]:

$$ahv = B(hv - E_g)^{\frac{1}{2}} \tag{7}$$

where α is the absorption coefficient, hv is the photon energy, E_g is the optical band gap energy, and B is an energy-independent constant with values between 1×10^5 and 1×10^6 cm^{-1} eV^{-1}. Fig. 10 depicts the Tauc's plot for band gap energy estimation where the E_g values were obtained at which the extrapolated linear part of $(\alpha h\nu)^2$ versus $h\nu$ plot intersects the energy x-axis. The E_g values are shown in Table 2. The E_g displayed a blue shift with increasing deposition time and initially increased from 3.260 eV to 3.290 eV as the deposition time increased to 3 min. The E_g value slightly decreased to 3.280 and 3.275 eV for 5 and 15 min deposition times, respectively. The variations in SnO_2 deposition time altered the E_g values, which may be associated with high band gap energy of the coated element, SnO_2 (3.6 eV), and also scattering effect at grain boundaries [46,47]. In addition, highly dense grain boundaries expedite the enhancement of potential barrier across the film, increasing the energy gap. The occurrence Burstein–Moss effect suggested that the shifting of E_g is associated with the increase of electron concentration filling the conduction band that causes the Fermi level to move higher than the band edge [48]. As mentioned before, Sn atoms at the interface of the heterojunction can diffuse into the ZnO structure as a dopant [39], considerably increasing free carrier concentration. According to Pauli's exclusion principle, states cannot be doubly occupied. Thus, the energy acquired by extra electrons increases, enabling them to jump from the valence band to the conduction band and thereby increasing the energy gap [49]. The E_g value was reduced after 15 min deposition possibly because of the increased thickness of the poor crystalline SnO_2 layer, increased scattering effect, and increased band tail states provided by the unrestrained diffusion of Sn into ZnO leading to shrinkage of the band gap [31,50].

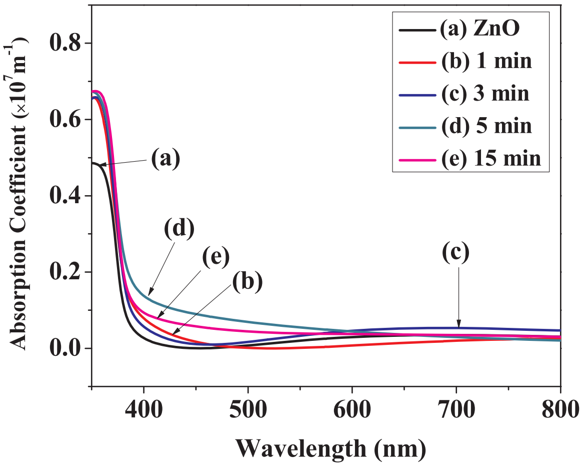

Fig. 9. Absorption coefficient of ZnO and SnO_2/ZnO heterojunction at different deposition times of SnO_2.

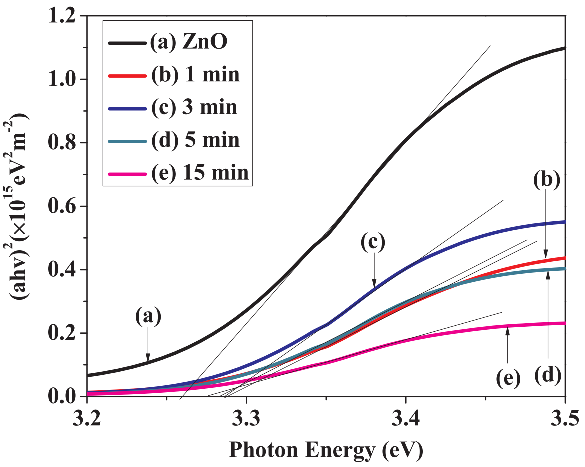

Fig. 10. Tauc's plot for band gap energy estimation of ZnO and SnO_2/ZnO heterojunction at different deposition times of SnO_2.

Near the optical band edge of the absorption coefficient curve, an exponential part named Urbach tail exists. This tail commonly emerges in poor crystalline, highly disordered, and amorphous materials because of the appearance of localized states, which increase the band gap. The density of the Urbach tail is represented by Urbach energy, E_u, which can be described by the following equation [51]:

$$\alpha = \alpha_0 \exp\left(\frac{hv}{E_u}\right) \tag{8}$$

where α is the absorption coefficient, α_0 is the pre-exponential factor, and hv is the photon energy. The variable E_u was denoted from the reciprocal gradient of the linear portion of ln (α) versus photon energy curve, as shown in Fig. 11. The E_u values that represent the density of film disorder are shown in Table 2. The increment of E_u is proportional to the increment of film stress, suggesting that increase in SnO_2 deposition time (thickness) generates a large structural disorder and enhances the residual stress through the film.

3.3. Resistance measurement

The influence of SnO_2 deposition time was analyzed from the I–V

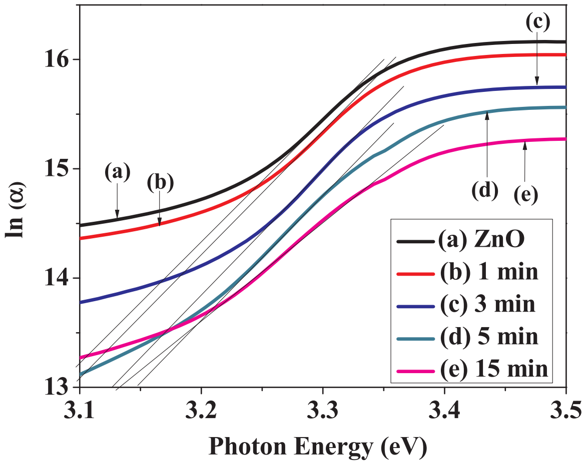

Fig. 11. Plot of ln (α) versus photon energy for ZnO and SnO_2/ZnO heterojunction at different deposition times of SnO_2.

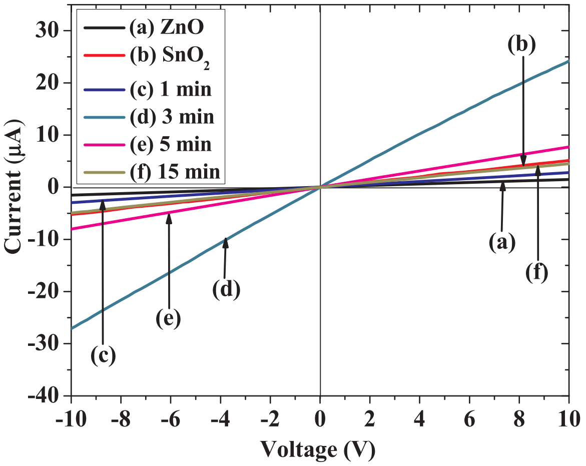

Fig. 12. I-V measurement of ZnO, SnO_2, and SnO_2/ZnO heterojunction at different deposition times of SnO_2.

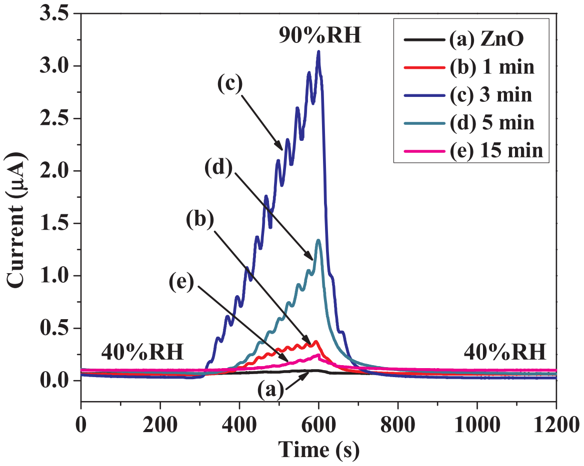

Fig. 13. Humidity sensing response of ZnO and SnO_2/ZnO heterojunction at different deposition times of SnO_2.

Table 3

Film resistance, $R_{a\text{-}40\%}$, $R_{rh\text{-}90\%}$, and sensitivity of ZnO and SnO_2/ZnO heterojunction films at different deposition times of SnO_2.

Sample	Film resistance (MΩ)	$R_{a\text{-}40\%}$ (MΩ)	$R_{rh\text{-}90\%}$ (MΩ)	Sensitivity
ZnO	6.74	74.0	52.2	1.42
1 min	3.75	85.9	15.1	5.69
3 min	0.40	144.0	1.59	90.56
5 min	1.32	73.5	3.73	19.71
15 min	2.11	50.1	20.3	2.47

measurement, as depicted in Fig. 12. The measurement was performed in ambient room temperature with a bias voltage ranging from − V to 10 V. The plot indicated that the films exhibited a linear increase of the current signal at varying bias voltages representing an Ohmic behavior. The measured resistance of each film is tabulated in Table 3. The film resistances of bare ZnO and SnO_2 films were measured to be 6.74 and 1.97 MΩ, respectively. The film resistance of SnO_2/ZnO heterojunction films was reduced compared with ZnO film. In addition, the film resistance of SnO_2/ZnO deposited with SnO_2 for 3 and 5 min are lower than that of the bare SnO_2 film. This decrease is suggested by the effective diffusion of the Sn^{4+} species into the ZnO lattice, which acts as a dopant, as mentioned earlier. As a result, the number of free carriers in the film increased, reducing film resistance. The film resistance increased after 3 min of SnO_2 deposition. In grain form, the nanoparticles encountered various deficiencies, such as high structural disorder and increase of grain boundaries. The increased thickness of the SnO_2, which has extremely small crystallite and grain size, considerably increased the grain boundaries, resulting in more carrier traps at the boundaries [52,53]. The carrier traps induced a potential barrier between the grains and restrained the movement of electrons between particles. This may induce poor electron mobility across the film. The decrease and increase in film resistance at certain SnO_2 thicknesses were also observed in other studies [54].

3.4. Humidity sensing performance

The humidity sensing performance levels of ZnO and SnO_2/ZnO films were investigated in a standard humidity chamber (ESPEC SH-261) with 5 V bias voltage and humidity level ranging from 40% RH to 90% RH. We fixed the measurement temperature to 25 °C to match the ambient condition. Fig. 13 displays the humidity-sensing responses, current versus time, at different humidity levels of the samples. The samples showed good response toward humidity changes with respect to adsorption (40–90% RH) and desorption (90–40% RH) processes, and current signal was stable at 40% RH before the elevation of humidity. The current signal steadily increased with increasing RH. The dehumidification process caused a rapid decrease in current signals, which continued to decline until a stable signal, as the initial state, was observed. The ZnO-based humidity sensor produced the lowest current changes (from 40% RH to 90% RH) among the heterojunction films, indicating that the composite structure successfully enhanced the humidity-sensing performance of the sensors. The 3 min deposition sample presented the largest changes in current, demonstrating an excellent sensitivity to humidity variations. Considering the ratio of current deviations, we estimated the sensitivity, S, of the humidity sensors to humidity, using the following relation [55]:

$$S = \frac{R_a}{R_{rh}} \tag{9}$$

where, R_a is the resistance at minimum humidity level (40% RH), and R_{rh} is resistance of the elevated humidity. The current signal attained from the plot was converted first to resistance by using Ohm's law ($V = IR$). The sensitivities of the films are listed in Table 3, and the sensitivity amendment over the disparity of humidity is shown in Fig. 14(a). The major aim of this scheme is to magnify the sensitivity of the intrinsic structure to humidity by determining an ideal thickness of the sensitizing (SnO_2) layer through the variations in SnO_2 deposition time. The sensitivity plots implied the dominant performance of the 3 min deposition sample, in which the sensitivity of each change in humidity level was more significant than those of the other samples. The sensitivity plot from 40% to 90% RH in Fig. 14(b) showed a clear trend of sensitivity enhancement induced by the variable deposition time for the SnO_2 layer. The sensitivity values improved with the appearance of SnO_2 layer from 1.42 of ZnO to 90.6 at 3 min deposition of SnO_2/ZnO. This result was attributed to several causes. First, during the preparation of SnO_2/ZnO bilayer films, some parts of the ZnO surface may have been dissolved to some degree by the acidic SnO_2 media and thus the actual surface area increased [56,57]. Second, according to the results of the XRD analysis, the formation of heterointerface between SnO_2 and ZnO led to the reduction of ZnO crystallite size, and this reduction promoted the enlargement of the surface area. Third, the possible diffusion of Sn atoms into the ZnO film at the interface increased free carrier concentration in the film, thereby increasing the electrostatic attraction of water molecules to the film surface [39]. Fourth, the improvement of sensing behavior corresponded to the homojunction interface between the adjacent SnO_2 grains. However, upon further increase in deposition times of SnO_2 above 3 min, the performance of the humidity sensors reduced at the sensitivity value of 2.47. This result is due to the increasing of series resistance on thicker SnO_2 nanoparticle layer, which decreases the generation of current value under humidity exposure. This result also consistent with the I-V measurement plot as

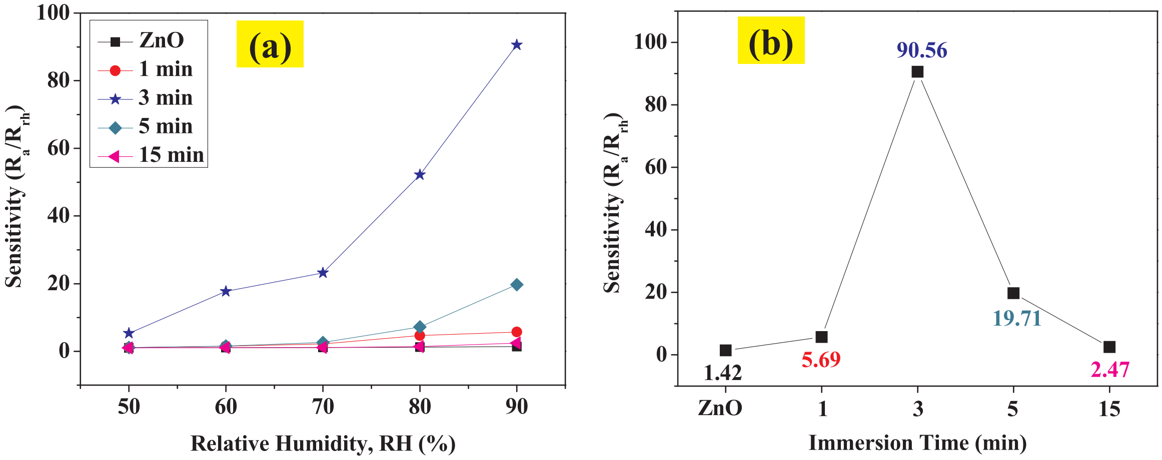

Fig. 14. (a) Sensitivity plot at different humidity level and (b) plot of sensitivity variation of ZnO and SnO_2/ZnO heterojunction at different deposition times of SnO_2.

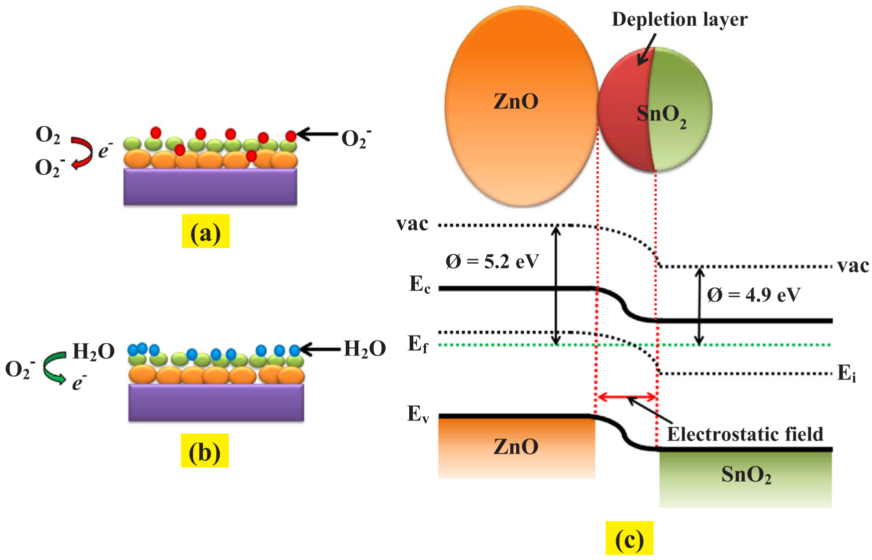

Fig. 15. Surface reactions of SnO_2/ZnO (a) without and (b) with humidity. (c) Energy band diagram of SnO_2/ZnO heterojunction.

discussed above. The obtained result is in agreement with previous research indicating that the increase of series resistance implies a suppression of the mobility of charge carriers due to the longer pathway [58,59]. Therefore, the current value decreases with increasing thickness of the SnO_2 nanoparticle layer. Subsequently, the sensitivity reduces after SnO_2 deposition above 3 min.

In air, oxygen molecules from the environment might have been attracted to the film surface, occupying the boundaries between the nanograins as in the reaction below [60].

$$O_2 + e^- \rightarrow O_2^- \tag{10}$$

Given the small grain size of SnO_2, many electrons were trapped. As a result, the potential barrier across the adjacent grains increased, thus reducing the concentration of free carriers in the heterojunction film. However, the heterojunction film benefits from this repercussion because the trapped electrons were released back to the film during the inception of water molecules to the sensor surface, as shown in the following reaction:

$$2H_2O + O_2^- \rightarrow 2H_2O_2 + e^- \tag{11}$$

This reaction results in the rapid change of current signal at variable humidity levels, improving the sensitivity of the sensors to humidity. During this condition, the current value increased linearly with the increase of RH through electronic conduction. When the sensors were exposed to higher RH level, the chemisorbed layer of water molecules is formed on the sensing surface due to dissociative chemisorption process [61]. Subsequently, the physisorbed layers are formed on the top of chemisorbed layer through hydrogen bonding. These physisorbed layers can decompose into H_3O^+ and OH^- ions due to high electrostatic field in the chemisorbed layer [26]. During this stage, the sensing mechanism is governed by ionic conduction, which increase the current response of the sensors. The SnO_2 nanoparticles on ZnO enhances the adsorption and desorption rates of the water molecules on the sensing surface due to the multiplicative effects of heterojunction composite and surface area enhancement. Hereafter, the sensitivity of the sensor improves with the SnO_2 nanoparticles. The surface reaction processes of SnO_2/ZnO heterojunction films without and with humidity are shown in Figs. 15(a) and 15(b), respectively. The last possible explanation for the sensitivity enhancement is the synergetic effect between SnO_2 and ZnO. When these two elements come into contact with each other, the electron from SnO_2 conduction band transferred to ZnO due to the difference of work function until their Fermi level reached equilibrium, as shown in Fig. 15(c) [62,63]. This phenomenon resulted in band bending and formation of depletion and accumulation layers between the materials [63]. The modulation of electron at the heterointerface caused the enhancement of the sensing properties and reduction of the possibility of electron–hole recombination. Such behavior was also reported in previous studies [64–66]. Moreover, the lowest film

Table 4
Comparison of the sensors based on heterojunctions and composites with different materials.

Sensing material	Sensor type	Range of RH (%)	Sensitivity	References
RGO-Fe: SnO_2	Resistive	0–100	3.23 [ΔR/R]	[67]
SnO_2/ZnO	Piezoelectric	5–95	76.4 [ΔV/V]	[68]
ZnO/MWCNTs/ZnO	Resistive	11–97	24.8 [ΔR/Δ% RH]	[69]
VO_2(B)@ZnO	Resistive	11–95	700 [$R_{11\%}/R_{95\%}$]	[70]
PPy-ZnO	Resistive	11–95	32.4 [ΔR/Δ% RH]	[71]
SnO_2/ZnO	Resistive	40–90	90.56 [$R_{a-40\%}/R_{rh-90\%}$]	This work

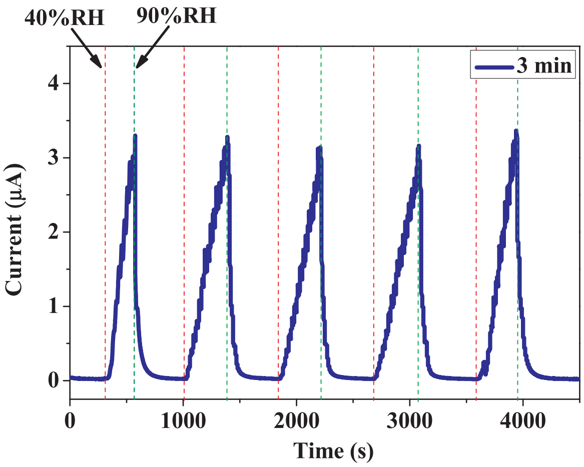

Fig. 16. Repeatability behavior of SnO_2/ZnO deposited with SnO_2 for 3 min.

resistance was observed during the 3 min SnO deposition, as shown in the I–V measurement results, which denoted that the sample had good electron transport properties and more free carrier than the other samples. The sensing performance levels of the sensors were slightly degraded when deposited for more than 3 min. As observed in the FESEM images, the ZnO and SnO_2/ZnO which deposited at low SnO_2 deposition times had rough surfaces. Increasing the deposition times of SnO_2 to some extent leads to the formation of a thicker, highly dense film and low roughness surface, which may reduce the surface interaction between water molecules and the sensing element. As a result, the active site for humidity adsorption is significantly reduced. Other than this observation, the increase of SnO_2 thickness may induce excessive grain boundaries, leading to the generation of higher interfacial states between the SnO_2–SnO_2 homojunction [40] and poor electron transport properties. Many studies investigated the use of ZnO heterojunction- and composite-based humidity sensors. The results from these studies are summarized in Table 4. Basing on these data, we concluded that the humidity sensing performance levels based on our study are comparable and superior to those obtained from previous reports.

Furthermore, we took the 3-min deposition sample with the highest sensitivity to humidity for further analysis. We measured the response of 3 min SnO_2/ZnO for five cycles to test the repeatability behavior of the sensor. The responses of the fabricated sensor was highly reproducible, as shown in Fig. 16. Nearly identical curves over five cycles were observed in the plot, indicating that the fabricated sensor of 3 min SnO_2/ZnO was very stable. In addition to the above, the humidity sensing response of 3 min SnO_2/ZnO was measured after one and six months to observe the stability of the device over a long period of time. The humidity sensing response of the sample after 1 and 6 months are depicted in Figs. 17 (a) and 17(b), respectively. From the humidity sensing response plot, the sensitivity values of the humidity sensor after 1 and 6 months were 89.92 and 90.29, respectively. The results show that the sensitivity values of the sensor after one and six month are nearly identical. The measurements indicated that the fabricated humidity sensor is highly stable for a particular period and applicable for long-term use.

4. Conclusion

SnO_2/ZnO heterojunction-based humidity sensors subjected to deposition with SnO_2 at varying times were fabricated through a two-step solution-based method, and the potential of SnO_2/ZnO as humidity sensor was analyzed. The surface areas of the ZnO films were enhanced when deposited with SnO_2. The enhancement was attributed to decreased grain size and crystallite size. Different deposition times have variable effects on transmittance properties. In particular, the E_g value slightly increased compared with ZnO. The film produced through the deposition of SnO_2 onto ZnO for 3 min had considerably reduced resistance. Furthermore, the bilayer sensors were critically dependent on deposition time. The films subjected to deposition for 3 min displayed had best performance with respect to humidity sensing, demonstrating

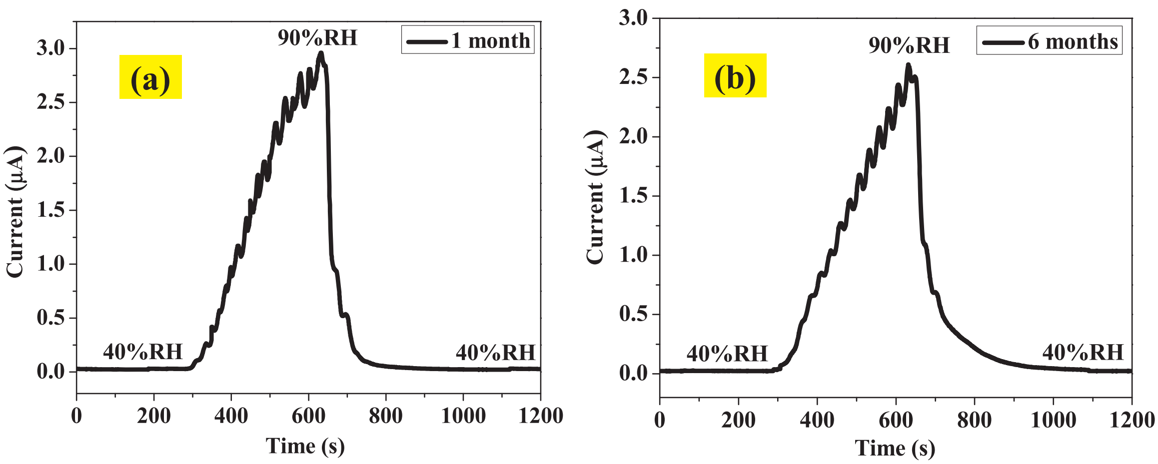

Fig. 17. Humidity sensing response of SnO_2/ZnO deposited with SnO_2 for 3 min measured after (a) 1 month and (b) 6 months.

a sensitivity value of 90.6, which was significantly higher than that of bare ZnO.

Acknowledgements

This work was supported by the GIP Grant (600-IRMI/MYRA 5/3/GIP (002/2017)). The authors also would like to thank the Institute of Research Management and Innovation (IRMI) of UiTM and the Ministry of Higher Education of Malaysia for their financial support of this research.

References

[1] Z. Chen, C. Lu, Humidity sensors: a review of materials and mechanisms, Sens. Lett. 3 (2005) 274–295.
[2] F.J. Arregui, Y. Liu, I.R. Matias, R.O. Claus, Optical fiber humidity sensor using a nano Fabry–Perot cavity formed by the ionic self-assembly method, Sens. Actuator B-Chem. 59 (1999) 54–59.
[3] C. Laville, J.Y. Delétage, C. Pellet, Humidity sensors for a pulmonary function diagnostic microsystem, Sens. Actuator B-Chem. 76 (2001) 304–309.
[4] R. Rimeika, D. Čiplys, V. Poderys, R. Rotomskis, M.S. Shur, Fast-response surface acoustic wave humidity sensor based on hematoporphyrin film, Sens. Actuator B-Chem. 137 (2009) 592–596.
[5] S. Akita, H. Sasaki, K. Watanabe, A. Seki, A humidity sensor based on a hetero-core optical fiber, Sens. Actuator B-Chem. 147 (2010) 385–391.
[6] A. Tételin, C. Pellet, C. Laville, G. N'Kaoua, Fast response humidity sensors for a medical microsystem, Sens. Actuator B-Chem. 91 (2003) 211–218.
[7] J.M. Corres, F.J. Arregui, I.R. Matías, Sensitivity optimization of tapered optical fiber humidity sensors by means of tuning the thickness of nanostructured sensitive coatings, Sens. Actuator B-Chem. 122 (2007) 442–449.
[8] Y. Kang, H. Ruan, Y. Wang, F.J. Arregui, I.R. Matias, R.O. Claus, Nanostructured optical fibre sensors for breathing airflow monitoring, Meas. Sci. Technol. 17 (2006) 1207.
[9] M. Folke, L. Cernerud, M. Ekström, B. Hök, Critical review of non-invasive respiratory monitoring in medical care, Med. Biol. Eng. Comput. 41 (2003) 377–383.
[10] B. Yang, B. Aksak, Q. Lin, M. Sitti, Compliant and low-cost humidity nanosensors using nanoporous polymer membranes, Sens. Actuator B-Chem. 114 (2006) 254–262.
[11] K. Shinghal, A. Noor, N. Srivastava, Intelligent humidity sensor for wireless sensor network agricultural application, Int. J. Wirel. Mob. Netw. 3 (2011) 118–128.
[12] K. Narimani, F.D. Nayeri, M. Kolahdouz, P. Ebrahimi, Fabrication, modeling and simulation of high sensitivity capacitive humidity sensors based on ZnO nanorods, Sens. Actuator B-Chem. 224 (2016) 338–343.
[13] L. Gu, K. Zheng, Y. Zhou, J. Li, X. Mo, G.R. Patzke, G. Chen, Humidity sensors based on ZnO/TiO2 core/shell nanorod arrays with enhanced sensitivity, Sens. Actuator B-Chem. 159 (2011) 1–7.
[14] J. Herrán, I. Fernández, E. Ochoteco, G. Cabañero, H. Grande, The role of water vapour in ZnO nanostructures for humidity sensing at room temperature, Sens. Actuator B-Chem. 198 (2014) 239–242.
[15] S.S. Batool, Z. Imran, M. Israr Qadir, M. Usman, H. Jamil, M.A. Rafiq, M.M. Hassan, M. Willander, Comparative analysis of Ti, Ni, and Au electrodes on characteristics of TiO2 nanofibers for humidity sensor application, J. Mater. Sci. Technol. 29 (2013) 411–414.
[16] V.K. Tomer, S. Duhan, A facile nanocasting synthesis of mesoporous Ag-doped SnO2 nanostructures with enhanced humidity sensing performance, Sens. Actuator B-Chem. 223 (2016) 750–760.
[17] E. Modaresinezhad, S. Darbari, Realization of a room-temperature/self-powered humidity sensor, based on ZnO nanosheets, Sens. Actuator B-Chem. 237 (2016) 358–366.
[18] G. Neri, A. Bonavita, S. Galvagno, N. Donato, A. Caddemi, Electrical characterization of Fe2O3 humidity sensors doped with Li+, Zn2+ and Au3+ ions, Sens. Actuator B-Chem. 111–112 (2005) 71–77.
[19] N.-F. Hsu, M. Chang, K.-T. Hsu, Rapid synthesis of ZnO dandelion-like nanostructures and their applications in humidity sensing and photocatalysis, Mater. Sci. Semicond. Process. 21 (2014) 200–205.
[20] S. Hussain, T. Liu, N. Aslam, S. Zhao, T. Li, D. Hou, W. Zeng, Assembly of bulbous ZnO nanorods to bulbous nanoflowers and their high selectivity towards formaldehyde, J. Mater. Sci. Mater. Electron. 27 (5) (2016) 4966–4971.
[21] S. Hussain, T. Liu, M. Kashif, L. Lin, S. Wu, W. Guo, W. Zeng, U. Hashim, Effects of reaction time on the morphological, structural, and gas sensing properties of ZnO nanostructures, Mater. Sci. Semicond. Process. 18 (2014) 52–58.
[22] B.A. Taleatu, E.A.A. Arbab, G.T. Mola, Synthesis and some surface studies of laminated ZnO/TiO2 transparent bilayer by two-step growth, Mater. Sci. Semicond. Process. 44 (2016) 85–90.
[23] M. Rani, S.K. Tripathi, Electron transfer properties of organic dye sensitized ZnO and ZnO/TiO2 photoanode for dye sensitized solar cells, Renew. Sustain. Energy Rev. 61 (2016) 97–107.
[24] S. Nam, J.-H. Yang, S.H. Cho, J.H. Choi, O.-S. Kwon, E.-S. Park, S.-J. Lee, K.-I. Cho, J. Jang, C.-S. Hwang, Solution-processed indium-free ZnO/SnO2 bilayer heterostructures as a low-temperature route to high-performance metal oxide thin-film transistors with excellent stabilities, J. Mater. Chem. C 4 (2016) 11298–11304.
[25] M.H. Mamat, M.F. Malek, N.N. Hafizah, M.N. Asiah, A.B. Suriani, A. Mohamed, N. Nafarizal, M.K. Ahmad, M. Rusop, Effect of oxygen flow rate on the ultraviolet sensing properties of zinc oxide nanocolumn arrays grown by radio frequency magnetron sputtering, Ceram. Int. 42 (2016) 4107–4119.
[26] A.S. Ismail, M.H. Mamat, N.D. Md. Sin, M.F. Malek, A.S. Zoolfakar, A.B. Suriani, A. Mohamed, M.K. Ahmad, M. Rusop, Fabrication of hierarchical Sn-doped ZnO nanorod arrays through sonicated sol–gel immersion for room temperature, resistive-type humidity sensor applications, Ceram. Int. 42 (2016) 9785–9795.
[27] N. Bhardwaj, S. Mohapatra, Structural, optical and gas sensing properties of Ag-SnO2 plasmonic nanocomposite thin films, Ceram. Int. 42 (2016) 17237–17242.
[28] K. Narimani, F.D. Nayeri, M. Kolahdouz, P. Ebrahimi, Fabrication, modeling and simulation of high sensitivity capacitive humidity sensors based on ZnO nanorods, Sens. Actuator B-Chem. 224 (2016) 338–343.
[29] S. Azad, E. Sadeghi, R. Parvizi, A. Mazaheri, Fast response relative humidity clad-modified multimode optical fiber sensor with hydrothermally dimension controlled ZnO nanorods, Mater. Sci. Semicond. Process. 66 (2017) 200–206.
[30] J. Jiang, L. Shi, T. Xie, D. Wang, Y. Lin, Study on the gas-sensitive properties for formaldehyde based on SnO2-ZnO heterostructure in UV excitation, Sens. Actuator B-Chem. 254 (2018) 863–871.
[31] S.-M. Lee, Y.-H. Joo, C.-I. Kim, Influences of film thickness and annealing temperature on properties of sol–gel derived ZnO–SnO2 nanocomposite thin film, Appl. Surf. Sci. 320 (2014) 494–501.
[32] D. Lu, Q. Gao, X. Wu, Y. Fan, ZnO nanostructures decorated hollow glass microspheres as near infrared reflective pigment, Ceram. Int. 43 (2017) 9164–9170.
[33] M.F. Malek, M.H. Mamat, M.Z. Musa, T. Soga, S.A. Rahman, S.A.H. Alrokayan, H.A. Khan, M. Rusop, Metamorphosis of strain/stress on optical band gap energy of ZAO thin films via manipulation of thermal annealing process, J. Lumines 160 (2015) 165–175.
[34] N. Manavizadeh, F.A. Boroumand, E. Asl-Soleimani, F. Raissi, S. Bagherzadeh, A. Khodayari, M.A. Rasouli, Influence of substrates on the structural and morphological properties of RF sputtered ITO thin films for photovoltaic application, Thin Solid Films 517 (2009) 2324–2327.
[35] M.N. Rezaie, N. Manavizadeh, E.M.N. Abadi, E. Nadimi, F.A. Boroumand, Comparison study of transparent RF-sputtered ITO/AZO and ITO/ZnO bilayers for near UV-OLED applications, Appl. Surf. Sci. 392 (2017) 549–556.
[36] D. Fang, K. Lin, T. Xue, C. Cui, X. Chen, P. Yao, H. Li, Influence of Al doping on structural and optical properties of Mg–Al co-doped ZnO thin films prepared by sol–gel method, J. Alloy. Compd. 589 (2014) 346–352.
[37] M.F. Malek, M.H. Mamat, M.Z. Musa, Z. Khusaimi, M.Z. Sahdan, A.B. Suriani, A. Ishak, I. Saurdi, S.A. Rahman, M. Rusop, Thermal annealing-induced formation of ZnO nanoparticles: minimum strain and stress ameliorate preferred c-axis orientation and crystal-growth properties, J. Alloy. Compd. 610 (2014) 575–588.
[38] B.-Z. Dong, G.-J. Fang, J.-F. Wang, W.-J. Guan, X.-Z. Zhao, Effect of thickness on structural, electrical, and optical properties of ZnO: Al films deposited by pulsed laser deposition, J. Appl. Phys. 101 (2007) 033713.
[39] W. Wang, S. Wang, X. Pan, Deposition and characterization of zinc oxide and tin oxide ultrafine particle bilayer thin films, Thin Solid Films 345 (1999) 212–216.
[40] I.J. Beyerlein, M.J. Demkowicz, A. Misra, B.P. Uberuaga, Defect-interface interactions, Prog. Mater. Sci. 74 (2015) 125–210.
[41] H.Q. Bian, S.Y. Ma, Z.M. Zhang, J.M. Gao, H.B. Zhu, Microstructure and Raman scattering of Ag-doping ZnO films deposited on buffer layers, J. Cryst. Growth 394 (2014) 132–136.
[42] D. Zhao, X. Wu, Nanoparticles assembled SnO2 nanosheet photocatalysts for wastewater purification, Mater. Lett. 210 (2018) 354–357.
[43] A. Muthukumar, G. Giusti, M. Jouvert, V. Consonni, D. Bellet, Fluorine-doped SnO2 thin films deposited on polymer substrate for flexible transparent electrodes, Thin Solid Films 545 (2013) 302–309.
[44] Y.-S. Kim, W.-P. Tai, S.-J. Shu, Effect of preheating temperature on structural and optical properties of ZnO thin films by sol–gel process, Thin Solid Films 491 (2005) 153–160.
[45] M.H. Mamat, M.Z. Sahdan, Z. Khusaimi, A.Z. Ahmed, S. Abdullah, M. Rusop, Influence of doping concentrations on the aluminum doped zinc oxide thin films properties for ultraviolet photoconductive sensor applications, Opt. Mater. 32 (6) (2010) 696–699.
[46] J. Rodríguez-Báez, A. Maldonado, G. Torres-Delgado, R. Castanedo-Pérez, MdlL. Olvera, Influence of the molar concentration and substrate temperature on fluorine-doped zinc oxide thin films chemically sprayed, Mater. Lett. 60 (2006) 1594–1598.
[47] A.P. Selvi Isabel, C.H. Kao, R.K. Mahanty, Y.C.S. Wu, C.Y. Li, C.Y. Lin, C.F. Lin, Sensing and structural properties of Ti-doped tin oxide (SnO2) membrane for biosensor applications, Ceram. Int. 43 (2017) 10386–10391.
[48] E. Burstein, Anomalous optical absorption limit in InSb, Phys. Rev. 93 (1954) 632–633.
[49] V. Shelke, B.K. Sonawane, M.P. Bhole, D.S. Patil, Electrical and optical properties of transparent conducting tin doped ZnO thin films, J. Mater. Sci. Mater. Electron. 23 (2) (2012) 451–456.
[50] F.Z. Bedia, A. Bedia, N. Maloufi, M. Aillerie, F. Genty, B. Benyoucef, Effect of tin doping on optical properties of nanostructured ZnO thin films grown by spray pyrolysis technique, J. Alloy. Compd. 616 (2014) 312–318.
[51] C. Shin, S.M. Iftiquar, J. Park, Y. Kim, S. Baek, J. Jang, M. Kim, J. Jung, Y. Lee, S. Kim, J. Yi, Optimization of intrinsic hydrogenated amorphous silicon deposited by very high-frequency plasma-enhanced chemical vapor deposition using the relationship between Urbach energy and silane depletion fraction for solar cell application, Thin Solid Films 547 (2013) 256–262.
[52] M. Boshta, F.A. Mahmoud, M.H. Sayed, Characterization of sprayed SnO2: Pd thin films for gas sensing applications, J. Ovonic Res. 6 (2010) 93–98.
[53] K. Ogata, K. Sakurai, S. Fujita, S. Fujita, K. Matsushige, Effects of thermal annealing

of ZnO layers grown by MBE, J. Cryst. Growth 214 (2000) 312–315.
[54] A.A. Yadav, Influence of film thickness on structural, optical, and electrical properties of spray deposited antimony doped SnO2 thin films, Thin Solid Films 591 (2015) 18–24.
[55] A.S. Ismail, M.H. Mamat, M.M. Yusoff, M.F. Malek, A.S. Zoolfakar, R.A. Rani, A.B. Suriani, A. Mohamed, M.K. Ahmad, M. Rusop, Enhanced humidity sensing performance using Sn-Doped ZnO nanorod Array/SnO2 nanowire hetero network fabricated via two-step solution immersion, Mater. Lett. 210 (2018) 258–262.
[56] S. Ito, Y. Makari, T. Kitamura, Y. Wada, S. Yanagida, Fabrication and characterization of mesoporous SnO2/ZnO-composite electrodes for efficient dye solar cells, J. Mater. Chem. 14 (2004) 385–390.
[57] A. Kay, M. Grätzel, Dye-sensitized core – shell nanocrystals: improved efficiency of mesoporous tin oxide electrodes coated with a thin layer of an insulating oxide, Chem. Mater. 14 (2002) 2930–2935.
[58] Y.-R. Li, C.-Y. Wan, C.-T. Chang, W.-L. Tsai, Y.-C. Huang, K.-Y. Wang, P.-Y. Yang, H.-C. Cheng, Thickness effect of NiO on the performance of ultraviolet sensors with p-NiO/n-ZnO nanowire heterojunction structure, Vacuum 118 (2015) 48–54.
[59] M.H. Mamat, N.I. Ishak, Z. Khusaimi, M.M. Zahidi, M.H. Abdullah, S. Muhamad, N.D.M. Sin, M.R. Mahmood, thickness-dependent characteristics of aluminium-doped zinc oxide nanorod-array-based, ultraviolet photoconductive sensors, Jpn. J. Appl. Phys. 51 (2012) 06FF03.
[60] C.-L. Hsu, K.-C. Chen, T.-Y. Tsai, T.-J. Hsueh, Fabrication of gas sensor based on p-type ZnO nanoparticles and n-type ZnO nanowires, Sens. Actuator B-Chem. 182 (2013) 190–196.
[61] S.K. Misra, N.K. Pandey, Analysis on activation energy and humidity sensing application of nanostructured SnO2-doped ZnO material, Sens. Actuator A-Phys. 249 (2016) 8–14.
[62] A. Kar, A. Patra, Recent development of core-shell SnO2 nanostructures and their potential applications, J. Mater. Chem. C 2 (2014) 6706–6722.
[63] Y. Fu, W. Zang, P. Wang, L. Xing, X. Xue, Y. Zhang, Portable room-temperature self-powered/active H2 sensor driven by human motion through piezoelectric screening effect, Nano Energy 8 (2014) 34–43.
[64] A. Katoch, S.-W. Choi, G.-J. Sun, S.S. Kim, An approach to detecting a reducing gas by radial modulation of electron-depleted shells in core-shell nanofibers, J. Mater. Chem. A 1 (2013) 13588–13596.
[65] A. Katoch, J.-H. Kim, Y.J. Kwon, H.W. Kim, S.S. Kim, Bifunctional sensing mechanism of SnO2–ZnO composite nanofibers for drastically Enhancing the sensing behavior in H2 gas, ACS Appl. Mater. Interfaces 7 (2015) 11351–11358.
[66] T. Rakshit, S. Santra, I. Manna, S.K. Ray, Enhanced sensitivity and selectivity of brush-like SnO2 nanowire/ZnO nanorod heterostructure based sensors for volatile organic compounds, RSC Adv. 4 (2014) 36749–36756.
[67] D. Toloman, A. Popa, M. Stan, C. Socaci, A.R. Biris, G. Katona, F. Tudorache, I. Petrila, F. Iacomi, Reduced graphene oxide decorated with Fe doped SnO2 nanoparticles for humidity sensor, Appl. Surf. Sci. 402 (2017) 410–417.
[68] D. Zhu, Y. Fu, W. Zang, Y. Zhao, L. Xing, X. Xue, Piezo/active humidity sensing of CeO2/ZnO and SnO2/ZnO nanoarray nanogenerators with high response and large detecting range, Sens. Actuator B-Chem. 205 (2014) 12–19.
[69] D. Zhang, N. Yin, B. Xia, Y. Sun, Y. Liao, Z. He, S. Hao, Humidity-sensing properties of hierarchical ZnO/MWCNTs/ZnO nanocomposite film sensor based on electrostatic layer-by-layer self-assembly, J. Mater. Sci. Mater. Electron. 27 (2016) 2481–2487.
[70] W. Li, Y. Ma, S. Ji, G. Sun, P. Jin, Synthesis and humidity sensing properties of the VO2(B)@ZnO heterostructured nanorods, Ceram. Int. 42 (2016) 9234–9240.
[71] R. Najjar, S. Nematdoust, A resistive-type humidity sensor based on polypyrrole and ZnO nanoparticles: hybrid polymers vis-a-vis nanocomposites, RSC Adv. 6 (2016) 112129–112139.